Geophysical Journal International

Geophys. J. Int. (2012) doi: 10.1111/j.1365-246X.2012.05518.x

Infrasound data inversion for atmospheric sounding

J.-M. Lalande,[1,2] O. Sèbe,[1] M. Landès,[1] Ph. Blanc-Benon,[2] R. S. Matoza,[3] A. Le Pichon[1] and E. Blanc[1]

[1] *CEA, DAM, DIF,* F91297, *Arpajon, France. E-mail: jeanmarie.lalande@gmail.com*
[2] *LMFA, UMR CNRS* 5509, *École Centrale Lyon, Université de Lyon,* 69134, *Ecully Cedex, France*
[3] *IGPP, Scripps Institution of Oceanography, University of California, San Diego, La Jolla, CA, USA*

Accepted 2012 April 19. Received 2012 January 26; in original form 2011 August 28

SUMMARY

The International Monitoring System (IMS) of the Comprehensive Nuclear-Test-Ban Treaty (CTBT) continuously records acoustic waves in the 0.01–10 Hz frequency band, known as infrasound. These waves propagate through the layered structure of the atmosphere. Coherent infrasonic waves are produced by a variety of anthropogenic and natural sources and their propagation is controlled by spatiotemporal variations of temperature and wind velocity. Natural stratification of atmospheric properties (e.g. temperature, density and winds) forms waveguides, allowing long-range propagation of infrasound waves. However, atmospheric specifications used in infrasound propagation modelling suffer from lack and sparsity of available data above an altitude of 50 km. As infrasound can propagate in the upper atmosphere up to 120 km, we assume that infrasonic data could be used for sounding the atmosphere, analogous to the use of seismic data to infer solid Earth structure and the use of hydroacoustic data to infer oceanic structure. We therefore develop an inversion scheme for vertical atmospheric wind profiles in the framework of an iterative linear inversion. The forward problem is treated in the high-frequency approximation using a Hamiltonian formulation and complete first-order ray perturbation theory is developed to construct the Fréchet derivatives matrix. We introduce a specific parametrization for the unknown model parameters based on Principal Component Analysis. Finally, our algorithm is tested on synthetic data cases spanning different seasonal periods and network configurations. The results show that our approach is suitable for infrasound atmospheric sounding on a regional scale.

Key words: Seismic monitoring and test-ban treaty verification; Wave propagation; Acoustic properties.

GJI Seismology

1 INTRODUCTION

The infrasound network of the International Monitoring System (IMS), deployed for verification of the Comprehensive Nuclear Test-Ban Treaty (CTBT), continuously records coherent infrasonic waves at the Earth's surface. Atmospheric infrasound can propagate over long range (from hundreds to thousands of kilometres) due to low attenuation (Bass *et al.* 1995; Sutherland & Bass 2004) and due to atmospheric ducts formed by temperature and wind variations with altitude (Drob *et al.* 2003).

Natural sources of infrasound include volcanic eruptions (Delclos *et al.* 1990; Garcés *et al.* 1999; Matoza *et al.* 2009; Fee *et al.* 2010), ocean swell (Le Pichon *et al.* 2004; Garcés *et al.* 2006), earthquakes (Mutschlecner & Whitaker 2005) and auroral activity (Wilson & Nichparenko 1967; Wilson 1969), and anthropogenic sources include supersonic aircraft (Balachandran *et al.* 1977; Le Pichon *et al.* 2002), chemical explosions (Ceranna *et al.* 2009) and mining blasts (Hagerty *et al.* 2002).

The increasing number of IMS infrasound arrays and additional arrays operated by research institutions allows new global-scale infrasound and atmospheric studies (Le Pichon *et al.* 2010). One of the major interests of the IMS infrasound network is the discrimination and characterization of different sources of infrasound, with the objective to detect atmospheric explosions anywhere on the Earth. Improvements in signal processing, source characterization and propagation modelling, together with an increasing amount of recorded data (Campus & Christie 2010) have considerably enlarged the scope of infrasound studies. Infrasound is valuable for monitoring volcanic activity, either by providing information in addition to seismometers (Matoza 2009) or as a remote monitoring technique when no seismic network is available (Matoza *et al.* 2011). Marty *et al.* (2010) have also demonstrated the capability of studying atmospheric gravity waves by means of the IMS infrasound network. In addition, it has been shown that continuous records of low-frequency acoustic waves can be used to improve understanding of atmospheric dynamics up to the lower thermosphere (Drob *et al.* 2003; Le Pichon *et al.* 2010).

The importance of accurate propagation modelling for infrasound studies has motivated the development of a variety of propagation models, for example, Tau-p ray tracing (Garcés *et al.* 1998),

normal modes (Pierce 1967), parabolic equation methods (Ostashev *et al.* 1997; Lingevitch *et al.* 2002), Finite-difference time-domain methods (de Groot-Hedlin 2008) and asymptotic methods which account for realistic 3-D atmospheres (Virieux *et al.* 2004; Dessa *et al.* 2005) and non-linear effects (Gainville *et al.* 2006).

Infrasound wave propagation modelling must be combined with accurate atmospheric specifications of temperature, wind velocities, density and molecular composition. Winds influence infrasound propagation by perturbing the background adiabatic sound speed in the direction of propagation resulting in an 'effective' sound speed (Pierce 1994), while wind components transverse to the direction of propagation deviate the wave front azimuth (Antier *et al.* 2007).

Atmospheric specifications dedicated to infrasound studies are constructed by combining numerical weather models for the lower atmosphere and empirical climatologies of the upper atmosphere. Atmospheric models up to 50 km altitude are provided directly by Numerical Weather Prediction (NWP) Centers (e.g. European Center for Medium Range Weather Forecasts and National Center for Environmental Prediction). They result from a rigorous statistical combination of fluid dynamic equations with observations (Kalnay *et al.* 1990; Hogan & Rosmond 1991; Courtier *et al.* 1998). Empirical climatologies are obtained by fitting data sets covering several decades to statistically describe wind fluctuations (Drob *et al.* 2008), temperature, density and molecular composition (Hedin 1991). These data sets include satellite observations of the middle and upper atmosphere and data from ground-based instruments such as lidars or radars (Hauchecorne *et al.* 2010). However, since observations above 50 km are sparse, empirical models only describe dominant seasonal to diurnal patterns and fail to capture fine-scale spatiotemporal structure related to meteorology. As infrasound can propagate at high altitudes (up to ∼120 km) through thermospheric and stratospheric ducts, significant and systematic bias has been observed (e.g. during seasonal transition) between observations and simulations (Donn & Rind 1971; Le Pichon *et al.* 2005a; Antier *et al.* 2007). It has been shown that wind corrections can be applied to improve agreement between observed and simulated data (Le Pichon *et al.* 2005b; Drob *et al.* 2010).

Extending this idea, we investigate the capability of infrasound observations for use as a remote sensing technique to improve the characterization of atmospheric properties in the mesosphere and lower thermosphere. Wave front parameters of coherent signals, such as trace-velocity, azimuth, traveltime or frequency can be estimated using array processing (Cansi 1995) and can be associated to a particular path in the atmosphere. These detected wave front characteristics can provide source localization estimation using backpropagation techniques. However, due to various levels of approximation (e.g. modelling theory, parametrization, data uncertainties and uncertainty in the atmospheric state) deviation from the actual source location is observed (Evers & Haak 2005; Matoza *et al.* 2011). To minimize the deviation between estimated and actual source location, we apply wind corrections to actual atmospheric specifications.

In this paper, wind corrections are applied on an iterative linear inversion scheme (Tarantola 2005) and adiabatic sound speed is assumed to be known. Although in practice multiple factors will control the feasibility of the infrasound data inversion (e.g. source characteristics, acquisition geometry, atmospheric specifications and data signal-to-noise ratios), here we focus on the effects of acquisition geometry (source–receiver geometry and number of infrasound receivers available) as well as the vertical complexity of atmospheric models.

2 INFRASOUND ATMOSPHERIC SOUNDING

The problem of retrieving meteorological parameters from infrasound observations is an inverse problem similar to seismic tomography (see Nolet 1987, for a review). The forward problem of infrasound propagation in the atmosphere is treated in the high-frequency approximation leading to the equations of ray trajectory along which the acoustic energy propagates.

As stated by Drob *et al.* (2010), we consider uncertainties associated with wind fields to be significantly higher than those of the temperature field, especially between the stratosphere and the lower thermosphere. Indeed, Drob *et al.* (2010) estimate the uncertainties of the adiabatic sound speed to be ∼1–3 m s^{-1} while uncertainties associated to wind velocities can easily reach ∼25–30 m s^{-1} above 50 km. Therefore, the inversion algorithm is developed to retrieve wind profiles assuming adiabatic sound speed is known.

2.1 Infrasound observables

Infrasound stations of the IMS network, recording infrasound waves at the Earth's surface, are composed of at least four microbarometric sensors in an array configuration. Array processing techniques are used to detect characteristics of coherent infrasound waves crossing an array (Cansi 1995). Typical infrasound observations are the trace velocity, the azimuth of the incoming wave front, the frequency content and the amplitude. Wave propagation traveltimes can be deduced when source origin time is known. The incidence angle of the wave front is related to the measured trace velocity v_t by the relation $\theta = \arcsin(v_t/c_0)$, where θ is measured with respect to the vertical axis and c_0 the effective sound speed at the Earth's surface. Thus, the vector of observed data, $\tilde{\mathbf{d}}$, should be noted,

$$\tilde{\mathbf{d}} = \{T^i, \theta^i, \phi^i\}, \tag{1}$$

where T^i, θ^i and ϕ^i are, respectively, the traveltime, the incidence angle and the azimuth of the ith detection.

In moving media, the reciprocity principles can be applied provided that wind components are reversed. According to this principle, sound signals propagating in opposite directions coincide so that source and receiver can be switched. Consequently, backpropagation of azimuth ϕ^i and incidence angle θ^i detected at a microbarometer array should reach the source location. In an inverse procedure, it is worthwhile to use the reciprocity principle and compute the traveltime T^i as a function of detected azimuths ϕ^i and incidence angles θ^i, as though the corresponding receiver were the source (Delprat-Jannaud & Lailly 1995). This way, the vector of observables could be transformed,

$$\mathbf{d} = \{T^i(\theta^i, \phi^i); \mathbf{s}\}, \tag{2}$$

where T^i is the traveltime of the ith detection and $\mathbf{s}$ the Cartesian components of the actual source location. This choice of infrasound observables avoids the eigenray computation usually required by tomographic problems (Julian & Gubbins 1977; Spiesberger & Worcester 1983), the source location being directly considered as data to be fitted. In addition, multiple paths (e.g. stratospheric and thermospheric paths) are easily handled in the inversion procedure (Delprat-Jannaud & Lailly 1995) as all simulated data are directly related to an observed azimuth and incidence angle.

2.2 Misfit function for infrasound atmospheric sounding

The general objective of the inverse problem is to retrieve a vector of model parameters $\mathbf{m}^*$ corresponding to a set of observables $\mathbf{d}_{\rm obs}$ such as,

$$\mathrm{g}(\mathbf{m}^*) = \mathbf{d}_{\rm obs}, \tag{3}$$

where g is the forward model operator computing the set of simulated data. The vector of model parameters is defined as the concatenation of zonal and meridional wind fields, $\mathbf{m} = \{v_x^k, v_y^k\}$, k being the number of parameters building the 1-D profiles. However, due to various levels of approximation in the forward model theory and uncertainties in the observed data, it is generally impossible to find a unique model $\mathbf{m}^*$ that strictly satisfies eq. (3). A common solution consists of finding the least-squares solution to the eq. (3). Defining a residual vector $\Delta\mathbf{d} = \mathbf{d}_{\rm obs} - \mathrm{g}(\mathbf{m})$ as the difference between observed and simulated data, the least-squares solution corresponds to model $\mathbf{m}$ minimizing the L_2-norm $\Delta\mathbf{d}^t\Delta\mathbf{d}$. Tarantola (2005) extended the inverse problem using a probabilistic point of view to overcome some limitations related to ill-conditioning, uncertainty considerations and non-unicity of the basic L_2-norm solution. In this formulation, model parameters, observations and forward theory are described by means of probability density functions. The solution of the inverse problem is, therefore, a posterior probability density function $\sigma(\mathbf{m}|\mathbf{d}_{\rm obs})$. Under the common assumption of Gaussian probability density functions, the maximum of $\sigma(\mathbf{m}|\mathbf{d}_{\rm obs})$ is the minimum of the misfit function,

$$\mathcal{C}(\mathbf{m}) = \Delta\mathbf{d}^t\mathbf{C}_{\rm D}^{-1}\Delta\mathbf{d} + \alpha\Delta\mathbf{m}^t\mathbf{C}_{\rm m}^{-1}\Delta\mathbf{m}, \tag{4}$$

where $\Delta\mathbf{m} = \mathbf{m} - \mathbf{m}_{\rm p}$ represents the difference between a vector $\mathbf{m}$ in the model space and $\mathbf{m}_{\rm p}$ the mean prior information on model parameters, $\mathbf{C}_{\rm D}$ and $\mathbf{C}_{\rm m}$ are the covariance matrices representing, respectively, data uncertainties and prior model uncertainties. The proper balance between data fit and model fit in eq. (4) is controlled by a weighting factor α and should be determined using the L-curve method (Hansen 1992).

According to eq. (2) described in Section 2.1, the residual vector $\Delta\mathbf{d}$ in eq. (4) quantifies both source position and traveltime residuals,

$$\Delta\mathbf{d} = \begin{bmatrix} s_x^{\rm act} - \mathbf{s}_x(\mathbf{m}) \\ s_y^{\rm act} - \mathbf{s}_y(\mathbf{m}) \\ \mathbf{t}_{\rm obs} - \mathbf{t}(\mathbf{m}) \end{bmatrix}, \tag{5}$$

where $s_x^{\rm act}, s_y^{\rm act}$ are the coordinates of the actual source location in the Cartesian plane, $\mathbf{s}_x(\mathbf{m}) = \{s_x^i\}$ and $\mathbf{s}_y(\mathbf{m}) = \{s_y^i\}$ are the simulated source location, $\mathbf{t}_{\rm obs} = \{t_{\rm obs}^i\}$ and $\mathbf{t}(\mathbf{m}) = \{t^i\}$ are the observed and simulated traveltimes and i corresponds to datum index.

Minimizing the objective function (4) leads to a weighted least-squares solution. This solution is equivalently obtained by iteratively solving, in the least-squares sense, the linear system (Monteiller *et al.* 2005),

$$\begin{bmatrix} -\mathbf{C}_{\rm D}^{-\frac{1}{2}}\mathbf{G}_c \\ \alpha^{\frac{1}{2}}\mathbf{C}_{\rm m}^{-\frac{1}{2}} \end{bmatrix}\delta\mathbf{m} = \begin{bmatrix} -\mathbf{C}_{\rm D}^{-\frac{1}{2}}\Delta\mathbf{d} \\ \alpha^{\frac{1}{2}}\mathbf{C}_{\rm m}^{-\frac{1}{2}}\Delta\mathbf{m} \end{bmatrix}, \tag{6}$$

where, $\delta\mathbf{m}$ is a model perturbation and $\mathbf{G}_c$ is the Fréchet derivatives matrix:

$$\mathbf{G}_c = \left[\frac{\partial\mathbf{g}^i}{\partial m_n}\right]_{\mathbf{m}_c}, \tag{7}$$

$\mathbf{g}^i = \{s_x^i; s_y^i; t^i\}$ being the simulation corresponding to datum i and n the index of model parameters. Data uncertainties are considered to be independent so that the covariance matrix $\mathbf{C}_{\rm D}$ is diagonal. We use the LSQR algorithm (Paige & Saunders 1982) in an iterative procedure to solve the system of linear eqs (6). This algorithm is similar to the conjugate gradients method and is particularly efficient for large sparse linear system. Other optimization algorithms, such as the Levenberg–Marquardt algorithm (Levenberg 1944; Marquardt 1963), could be used to minimize the objective function (4). This algorithm uses a line-search method to scale the gradient of eq. (4) by a factor either denoted α or λ in the literature. This factor belongs to the optimization procedure and is independent of the weighting factor α of eq. (4).

2.3 Forward problem: infrasound propagation modelling

Infrasound wave propagation is treated in the high-frequency approximation for computational efficiency and because it permits handling 3-D geometry. The forward problem is supplemented with two sets of perturbed equations derived from the ray trajectory equations. First, we consider perturbation of ray trajectory due to perturbations of initial conditions leading to the paraxial equations. Paraxial equations are used to compute synthetic data given some positions of source and infrasound arrays. We derive a second set of perturbed equations applying unit perturbation of wind parameters.

2.3.1 Ray tracing theory background

The high-frequency approximation to the wave equation leads to the eikonal equation for the traveltime wave fronts (Virieux *et al.* 2004),

$$(\nabla T)^2 = \frac{1}{c^2(\mathbf{q})}\left(1 - \mathbf{v}(\mathbf{q})\ .\ \nabla T\right)^2, \tag{8}$$

where T is the traveltime of the wave front. The eikonal eq. (8) is a non-linear second-order differential equation which can be solved by the method of characteristics (Courant & Hilbert 1989). Position $\mathbf{q}$ and slowness vector $\mathbf{p} = \nabla T$ are solutions of the differential equations (Whitham 1999):

$$\begin{aligned} \frac{\mathrm{d}q_i}{\mathrm{d}\tau} &= \frac{\partial\mathcal{H}}{\partial p_i} \\ \frac{\mathrm{d}p_i}{\mathrm{d}\tau} &= -\frac{\partial\mathcal{H}}{\partial q_i}, \end{aligned} \tag{9}$$

with the Hamiltonian,

$$\mathcal{H}(\mathbf{q},\mathbf{p}) = 1/2\left[\mathbf{p}^2 - u^2(\mathbf{q})(1 - \mathbf{p}.\mathbf{v}(\mathbf{q}))^2\right]\cdot \tag{10}$$

System (9) defines the ray trajectory equations, with $\mathcal{H}(\mathbf{q},\mathbf{p})$ the Hamiltonian function and u the sound slowness defined as the inverse of sound speed $u = 1/c$. The conservation law, $\mathcal{H} = 0$, emerging from the eikonal eq. (8) must be satisfied along the whole ray trajectory and is used to initialize the system of ray equations.

The sampling parameter along the ray trajectory τ depends on the chosen Hamiltonian $\mathcal{H}$. It could be an arc length along the ray or the time. Here, it has a more complex meaning which can be defined using the expression of traveltime in the Lagrangian formulation:

$$T = \int_{R(\mathbf{m})}\frac{\mathrm{d}s}{c + \mathbf{v}.\mathbf{n}}, \tag{11}$$

where ds represents the curvilinear coordinate and $R(\mathbf{m})$ is the ray trajectory. In the Hamiltonian formulation, the expression for

traveltime is given by

$$T = \int_{R(\mathbf{m})} (\mathbf{p}.\dot{\mathbf{q}} - \mathcal{H})\, \mathrm{d}\tau, \tag{12}$$

where $\dot{\mathbf{q}} = \mathrm{d}\mathbf{q}/\mathrm{d}\tau$. The relation between the sampling parameter τ and the arc length ds along the ray is obtained by straightforward analysis and leads to,

$$\mathrm{d}\tau = c(\mathbf{q})\mathrm{d}s\cdot \tag{13}$$

The sampling parameter $d\tau$ has the dimension of a velocity multiplied by a distance. This formulation of the sampling parameter is convenient because the distance along the ray path is automatically reduced when the local sound speed increases. The differential eqs (9) are solved in the Cartesian coordinate system using the Adams–Bashforth–Moulton multistep solver (Shampine & Gordon 1975). This method allows a rapid and accurate computation by controlling the local truncation error along the ray trajectory. The ray computation accuracy can be controlled by verifying the nullity of the Hamiltonian along the ray trajectory. A sampling parameter of $\mathrm{d}\tau = 0.02\ \mathrm{m^2 s^{-1}}$ has been shown to give satisfying accuracy for our purposes.

2.3.2 Paraxial equations

Paraxial equations are derived from perturbations of initial conditions $\mathbf{q}_0$ and $\mathbf{p}_0$. Given a slightly perturbed position $\mathbf{q}_0 + \delta\mathbf{q}$ and slowness vector $\mathbf{p}_0 + \delta\mathbf{p}$, the resulting Hamiltonian perturbation is $\mathcal{H}_0 + \left(\partial_{\mathbf{q}}\mathcal{H}\right)_0 .\delta\mathbf{q} + \left(\partial_{\mathbf{p}}\mathcal{H}\right)_0 .\delta\mathbf{p}$, where $\mathcal{H}_0$ indicates computation along the unperturbed ray. In the following, we denote phase space perturbed coordinates $\delta\mathbf{y} = (\delta\mathbf{q}, \delta\mathbf{p})$ and $\dot{\delta\mathbf{y}} = (\mathrm{d}\delta\mathbf{q}/\mathrm{d}\tau, \mathrm{d}\delta\mathbf{p}/\mathrm{d}\tau)$. Thus, the linearized system of perturbed equations is,

$$\dot{\delta\mathbf{y}}(\tau) = \mathbf{H}_0(\tau)\delta\mathbf{y}(\tau), \tag{14}$$

with

$$\mathbf{H}_0 = \begin{bmatrix} \nabla_p\nabla_q\mathcal{H}_0 & \nabla_p\nabla_p\mathcal{H}_0 \\ -\nabla_q\nabla_q\mathcal{H}_0 & -\nabla_q\nabla_p\mathcal{H}_0 \end{bmatrix}_0 . \tag{15}$$

Eq. (14) is a homogeneous system of equations which is solved efficiently by the propagator matrix method (Aki & Richards 1980). The partial derivatives of the Hamiltonian function have been calculated in Virieux *et al.* (2004) and Dessa *et al.* (2005) and are recalled in the Appendix.

2.3.3 First-order perturbation theory due to change in wind model

The computation of ray perturbation due to a change in the atmospheric model is performed using an approach equivalent to the derivation of paraxial equations (Farra *et al.* 1989). Let us consider a slight perturbation of the wind model $\mathbf{v}(\mathbf{q}) = \mathbf{v}_0(\mathbf{q}) + \delta\mathbf{v}$. This perturbation generates a perturbation of the Hamiltonian function $\mathcal{H} = \mathcal{H}_0 + \Delta\mathcal{H}$, subscript 0 indicating computation along the reference unperturbed ray. A first-order analysis leads to the perturbed Hamiltonian,

$$\Delta\mathcal{H} = u_0^2(\mathbf{q})\,(\mathbf{p}_0 \,.\, \delta\mathbf{v})[1 - \mathbf{p}_0 \,.\, \mathbf{v}_0(\mathbf{q})] + o(\delta\mathbf{v}^2)\cdot \tag{16}$$

The system of perturbed equations becomes,

$$\dot{\delta\mathbf{y}}(\tau) = \mathbf{H}_0(\tau)\delta\mathbf{y}(\tau) + \Delta\mathbf{H}(\tau), \tag{17}$$

where,

$$\Delta\mathbf{H} = \begin{pmatrix} \frac{\partial\Delta\mathcal{H}}{\partial p_i} \\ -\frac{\partial\Delta\mathcal{H}}{\partial q_i} \end{pmatrix} . \tag{18}$$

This system of equations is similar to the paraxial system of eqs (14) with a source term $\Delta\mathcal{H}$. Eq. (17) is also solved by standard propagator methods (Aki & Richards 1980; Farra *et al.* 1989). Expressions of partial derivatives are given in the Appendix.

2.3.4 Reflection and transmission at an interface

The equations defined in Sections 2.3.2 and 2.3.3 are valid for continuous atmospheric properties. This condition breaks down when rays intersect the Earth's surface, and reflection conditions must be matched at the interface (Candel 1977; Farra *et al.* 1989). Reflection and transmission of perturbed rays due to perturbations of initial conditions and wind model perturbations must be considered with care as perturbed rays may not reach the ground interface with the same sampling parameter τ as the reference ray (Fig. 1). For a ray reaching the interface at sampling parameter τ_i with phase coordinates $\mathbf{y}_0(\tau_i) = (\mathbf{q}_0, \mathbf{p}_0)$, the perturbed ray will intersect the same interface at sampling parameter τ_i' and phase coordinates $\mathbf{y}'(\tau_i') = (\mathbf{q}', \mathbf{p}')$. In general, τ_i and τ_i' will not coincide, so that paraxial or perturbed rays have to be projected over the interface. We denote by $\delta\mathbf{q} = \mathbf{q}'(\tau_i) - \mathbf{q}_0(\tau_i)$ and $\delta\mathbf{p} = \mathbf{p}'(\tau_i) - \mathbf{p}_0(\tau_i)$ the deviation between unperturbed and perturbed rays at equal sampling parameter τ_i. The computation of $\delta\mathbf{y} = (\delta\mathbf{x}, \delta\mathbf{p})$ results from eqs (14) or (17). Deviation $d\mathbf{q} = \mathbf{q}'(\tau_i') - \mathbf{q}_0(\tau_i)$ and $d\mathbf{p} = \mathbf{p}'(\tau_i') - \mathbf{p}_0(\tau_i)$ between unperturbed and perturbed ray at the interface are computed using reflection conditions for the perturbed ray. We also introduce phase coordinates $d\mathbf{y} = (d\mathbf{q}, d\mathbf{p})$. The reflection and transmission of perturbed ray coordinates at the ground surface are given by

$$d\hat{\mathbf{y}}(\tau_i') = \mathcal{T}\mathcal{R}\delta\mathbf{y}(\tau_i), \tag{19}$$

where the hat symbol refers to phase coordinates in the transmitted medium, and $\mathcal{T}$ and $\mathcal{R}$ are linear operators of the form,

$$\mathcal{T} = \begin{bmatrix} I & 0 \\ \mathcal{T}_1 & \mathcal{T}_2 \end{bmatrix}, \tag{20}$$

and,

$$\mathcal{R} = \begin{bmatrix} \mathcal{R}_1 & 0 \\ \mathcal{R}_2 & I \end{bmatrix} . \tag{21}$$

$\mathcal{T}$ and $\mathcal{R}$ are 6×6 matrices whose elements are developed in Farra *et al.* (1989). Reflection and transmission operators applied to perturbed rays have the same expression whether we slightly perturb the initial conditions or the wind model. The only exception arises when the wind model is perturbed in the vicinity of the source. In this case, a perturbation of the initial slowness vector $\mathbf{p}_i$ has to be taken into account to satisfy the conservation equation $\mathcal{H} = 0$ (Farra *et al.* 1989). However, due to the extreme sensitivity of the ray trajectory to initial conditions, we hold the wind model unchanged in the lowermost ∼18–25 km during the inversion procedure, so that we do not need to derive these special conditions in the forward model.

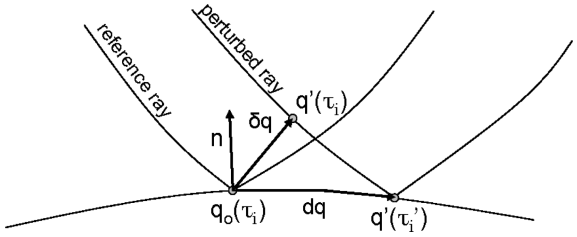

Figure 1. Geometry of the reflection of a reference ray and a perturbed ray at an interface.

2.3.5 Forward problem parametrization

The ray eqs (9) require the estimation of local sound and wind velocity and their first spatial derivatives, and, systems (14) and (17) require also the second spatial derivatives. We consequently need an analytic representation of wind profiles (Virieux & Farra 1991; Virieux *et al.* 2004). A convenient way to describe the atmospheric models is to use polynomial parametric curves such as B-spline basis functions (De Boor 1978). A B-spline curve of degree p satisfies the locality property, as only $p+1$ points (the control polygon) are needed to compute each segment of the interpolation curve of the entire 1-D profile. Moreover, computation of local sound and wind velocities as well as their nth spatial derivatives are achieved very efficiently due to pre-computed B-spline functions. To satisfy the continuity of the second-order derivative of sound speed and wind fields, B-splines of degree 3 are used leading to a local control polygon composed of four points.

2.3.6 Characteristics of infrasound propagation

The forward model described in Section 2.3.1 is used to illustrate atmospheric wave propagation with HWM07-MSIS profiles (Hedin 1991; Drob *et al.* 2008) on January 1 12H00 UTC and geographical coordinates 20.85°S,168.14°E (Fig. 2). Acoustic ray simulation are performed with a source at $(x, y, z) = (0, 0, 0)$ and a grid spanning [0°–360°] in azimuth and [30°–85°] in incidence angle, with uniform sampling step of 0.25° in incidence and azimuth. Fig. 3 shows ray endpoints at the ground surface colour coded according to the turning point altitude. The acoustic energy is ducted between the ground and both ∼45–55 km and ∼110–130 km. Refracting paths at ∼110–130 km correspond to thermospheric arrivals (*It*) and are observed in all azimuthal directions, while stratospheric arrivals (*Is*) refracted at approximately ∼45–50 km are observed west from the source in the direction of the stratospheric wind jet. Fast stratospheric arrivals *Isf* (Evers & Haak 2007) are also modelled northwest from the source. Thermospheric paths are quite stable on seasonal timescales but major changes occur at the diurnal scale due to successive cooling and heating in the thermosphere. Stratospheric waves are usually stable during a season due to the stationarity of the stratospheric wind jet. However, they strongly depend on stratospheric wind jet reversals.

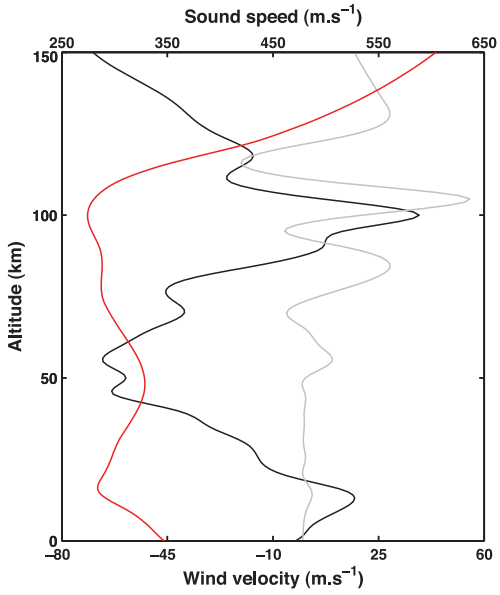

Figure 2. HWM07-MSIS atmospheric sound speed (red line), zonal wind velocity (black line) and meridional wind velocity (grey line) for austral summer (January 1 12H00 UTC) at geographical coordinates 20.85°S,168.14°E.

3 CONSTRUCTION OF THE FRÉCHET DERIVATIVES MATRIX

This section details the construction of the Fréchet derivatives matrix (7) needed for the resolution of the system (6) in the iterative least-squares sense.

3.1 Sensitivity of the forward model to wind parameters

The Fréchet derivatives matrix, $\mathbf{G}_c$, is the matrix of partial derivatives of the forward model outputs with respect to model parameters. It is constructed using the ray perturbed eq. (17) and reflection condition (21) for partial derivatives of estimated source position and the derivative of traveltime. The differential expression for traveltime at sampling parameter τ is given by,

$$\Delta T(\tau) = [\mathbf{p}_0.\mathrm{d}\mathbf{q}]_{\tau_0}^{\tau} - \int_{\tau_0}^{\tau} \Delta H \mathrm{d}\tau, \tag{22}$$

where ΔH is the perturbed hamiltonian of eq. (16).

In the following, we denote τ^i_{grd} the sampling parameter at which the reference ray intersects the ground surface. The expressions of partial derivatives for unit perturbation of wind field are given by

$$\frac{\partial s_x^i}{\partial m_n} = \mathcal{R}\delta q_x^i\left(\tau^i_{\mathrm{grd}}; \delta m_n\right), \tag{23}$$

$$\frac{\partial s_y^i}{\partial m_n} = \mathcal{R}\delta q_y^i\left(\tau^i_{\mathrm{grd}}; \delta m_n\right), \tag{24}$$

$$\frac{\partial T^i}{\partial m_n} = \Delta T^i\left(\tau^i_{\mathrm{grd}}; \delta m_n\right), \tag{25}$$

where δq_x^i and δq_y^i are elements of the perturbed phase coordinates given by the system (17) and i refers to each observation. Reflection conditions are also applied by multiplication with matrix $\mathcal{R}$. Vector $m_n = \{v_x^k; v_y^k\}$ stands for the set of model parameters with $n = 1, \ldots, 2k$, k the number of model parameters per wind field, and δm_n is a unitary perturbation of the nth component of the wind field. In these equations, local wind velocity and sound speed are interpolated using B-spline functions.

3.2 Inverse problem parametrization: a modified Fréchet derivatives matrix

The spatiotemporal variability of atmospheric parameters can be successfully described using principal component analysis (PCA; Williams 1997; Bordoni & Stevens 2006) or other related dimensionality reduction methods. These methods are useful to find both temporal and spatial patterns in a data set. Similar to ocean acoustic tomography (Munk *et al.* 1995), we apply PCA to horizontal wind model time-series to reduce the number of unknowns describing the model. Let us denote by $\mathbf{m}^\beta$ a set of 1-D wind profiles with $\beta = \{1, \ldots, N\}$ the index of profiles and N is the number of profiles. The projection of the data set, $\mathbf{m}^\beta$, in a linear orthogonal subspace, is written,

$$\mathbf{m}^\beta = \mathbf{W}\boldsymbol{\eta}^\beta + \boldsymbol{\mu} + \boldsymbol{\epsilon}, \tag{26}$$

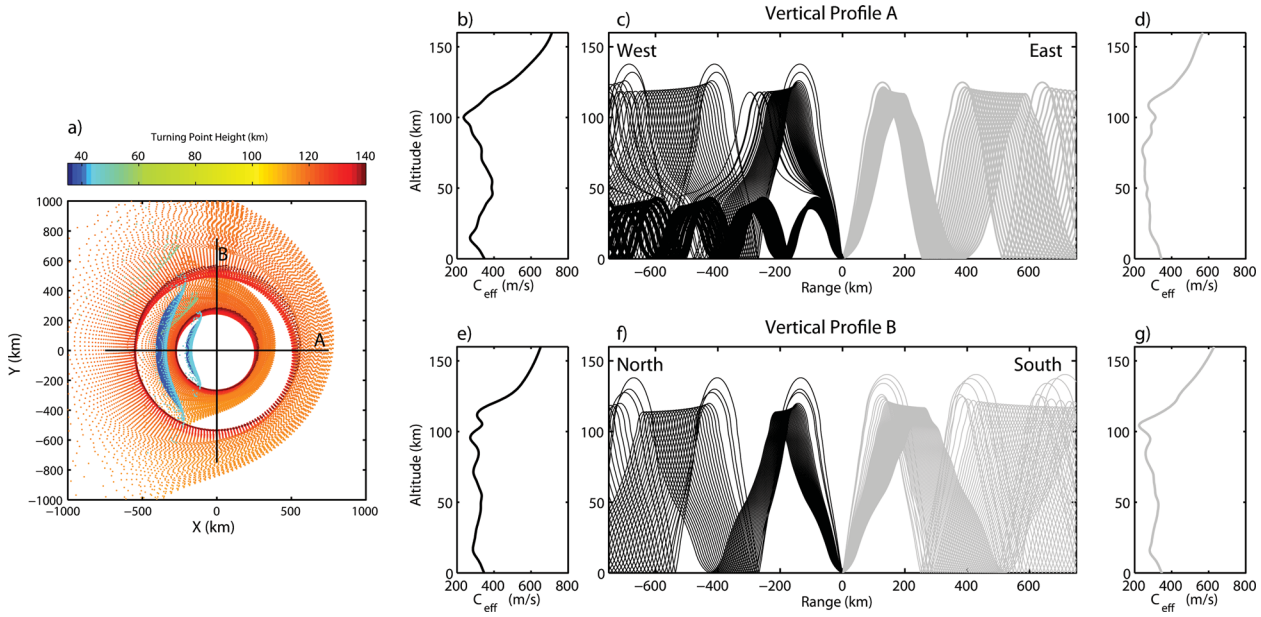

Figure 3. Infrasound ray tracing simulation. (a) Map of ray endpoints, (b) westward effective soundspeed, (c) ray tracing in east–west profile A, (d) eastward effective sound speed, (e) northward effective sound speed, (f) ray tracing in north–south direction and (g) southward effective soundspeed.

where $\mathbf{W}$ is the matrix of orthogonal basis functions (OBFs), defined by PCA, whose elements are $W_{ij} = \phi^i(z_j)$, and $\phi^i(z)$ are the OBFs, $\boldsymbol{\eta}^\beta$ are the variables in the OBF, the vector $\boldsymbol{\mu}$ is the average of the data set and $\boldsymbol{\epsilon}$ is a noise vector. Variables $\boldsymbol{\eta}^\beta$ are commonly called latent variables. OBFs are defined as the eigenvectors of the covariance matrix:

$$S_{ij} = \frac{\sum_{\beta=1}^{N} \left(m_i^\beta - \mu_j^\beta\right)\left(m_j^\beta - \mu_j^\beta\right)^t}{N}, \tag{27}$$

where $i = j = \{1, \ldots, n\}$ represent altitude indices and n the number of parameters in the 1-D profiles. Since most of the variance in the data set is contained in the first principal axis, the OBF $\mathbf{W}$ can be truncated to reduce the number of explanatory variables.

PCA is performed on the HWM07 (Drob *et al.* 2008) and NRLG2S (Drob *et al.* 2003) atmospheric specifications used for synthetic inversion in Section 4. HWM07 is an empirical horizontal wind model describing dominant diurnal to seasonal patterns of the atmosphere, while NRLG2S is a global hybrid spectral model combining NWP models of the lower atmosphere with empirical models of the upper atmosphere, such as HWM93 (Hedin *et al.* 1996) or HWM07. Here, NRLG2S is combined with the HWM93 specification. NWP models provide detailed descriptions of the atmosphere up to ∼50 km based on fluid dynamic equations.

A 1-yr time-series of HWM07 and a 4-yr time-series (2003–2007) of NRLG2S at geographical coordinates 20.85°S, 168.14°E constitute the data set used for the PCA. Fig. 4 shows the first four OBFs obtained with HWM07 and NRLG2S specifications, while Fig. 5 shows the total L_2-norm error of the reconstructed time-series as a function of the number of latent variables used for the reconstruction.

OBFs of the first mode display similar behaviour for HWM07 and NRLG2S specification. For instance, the first mode of zonal component characterizes the variance in the stratospheric wind jet. Major differences between OBFs associated with HWM07 and NRLG2S specifications occur in the higher modes.

The total L_2-norm error of reconstructed HWM07 zonal and meridional wind profiles does not decrease beyond the 23rd OBF, while for NRLG2S profiles the decrease in total L_2-norm error is continuous and more OBFs are required to obtain comparable error. Latent variables in the OBF space are used as control variables of the inverse problem instead of the n control points describing each wind component.

We use (23)–(25) and the derivative of model parameters with respect to latent variables, $\partial m_n / \partial \eta_l = W_{nl}$, to obtain the derivatives of position and traveltime with respect to linear coefficient of the OBF are

$$\frac{\partial s_x^i}{\partial \eta_l} = \frac{\partial s_x^i}{\partial m_n}\frac{\partial m_n}{\partial \eta_l} = \mathcal{R}\delta q_x^i\left(\tau_{\text{grd}}^i; \delta m_n\right) W_{nl}, \tag{28}$$

$$\frac{\partial s_y^i}{\partial \eta_l} = \frac{\partial s_y^i}{\partial m_n}\frac{\partial m_n}{\partial \eta_l} = \mathcal{R}\delta q_y^i\left(\tau_{\text{grd}}^i; \delta m_n\right) W_{nl}, \tag{29}$$

$$\frac{\partial T^i}{\partial \eta_l} = \frac{\partial T^i}{\partial m_n}\frac{\partial m_n}{\partial \eta_l} = \Delta T^i\left(\tau_{\text{grd}}^i; \delta m_n\right) W_{nl}, \tag{30}$$

where l is the index of OBF and $l < n$ such that W_{nl} represents the truncated basis functions.

4 SYNTHETIC INVERSION EXPERIMENT

In this section, the inversion algorithm is validated and performance is evaluated on a set of synthetic data cases. The synthetic data are chosen to investigate key features of infrasonic atmospheric sounding.

4.1 Details on synthetic data

Synthetic data sets are generated using the forward model described in Section 2.3.1 for different synthetic infrasound network configurations and atmospheric specifications. Atmospheric

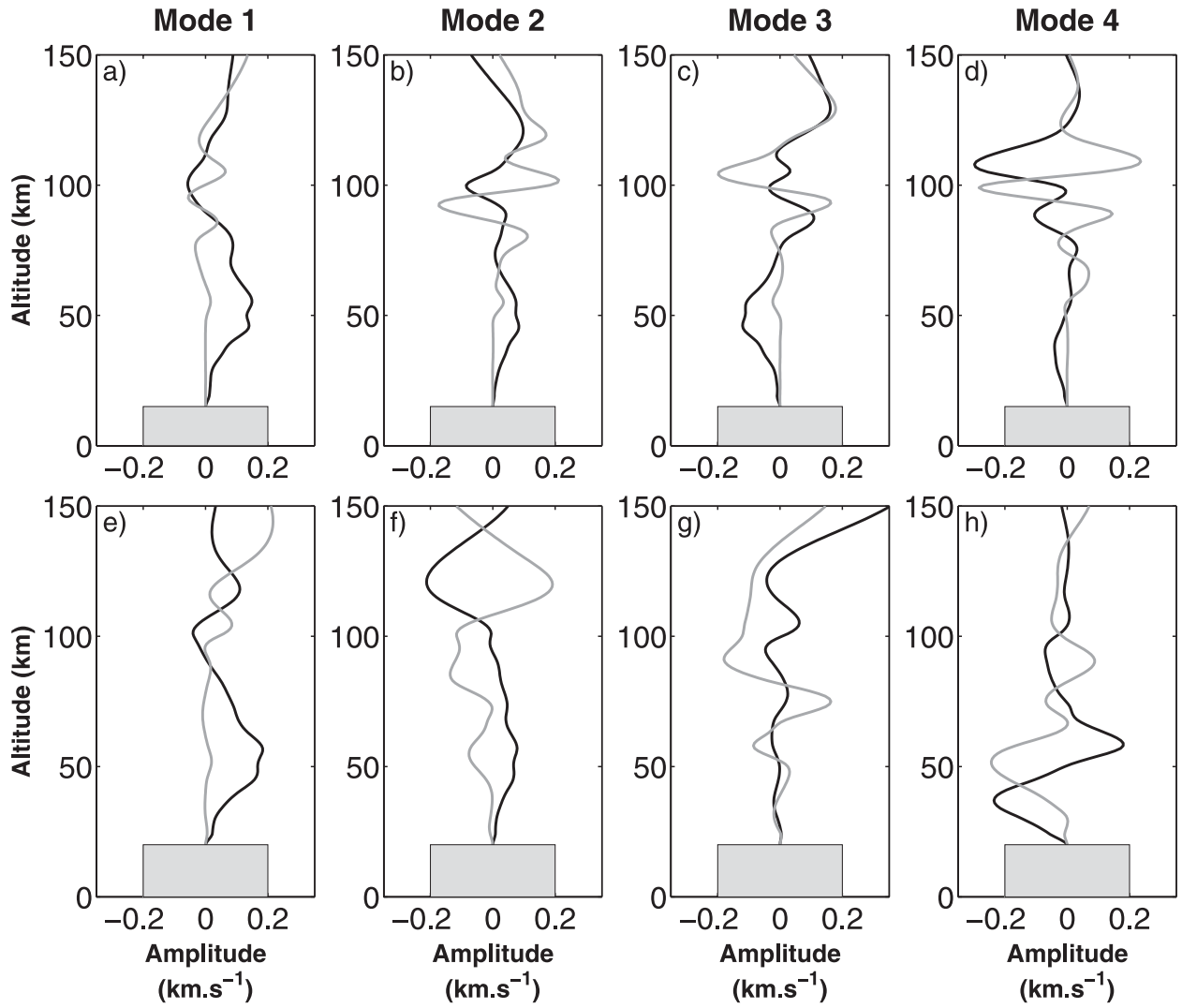

Figure 4. Orthogonal basis function (OBF) obtained by PCA analysis of 1-D profile time-series at geographical coordinates 20.85°S,168.14°E. (a–d) OBFs associated to HWM07 specifications: (a)–(d) correspond, respectively, to modes 1, 2, 3 and 4 (decreasing order of associated eigenvalues). (e–h) same as (a-d) for NRLG2S specification. Dark lines correspond to zonal wind OBF and grey lines to meridional wind OBF. Grey rectangles correspond to the section of wind profiles not inverted.

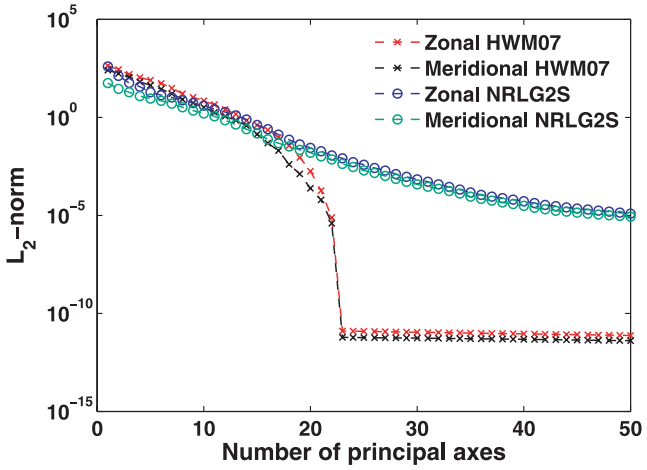

Figure 5. Total L_2-norm error of the reconstructed profiles depending on the atmospheric specification versus the number of axes used for the reconstruction.

conditions correspond to austral summer, January 1 12H00 UTC, for HWM07 (Fig. 8a) and NRLG2S (Fig. 9a), and equinox conditions, October 28 12H00 UTC, for HWM07 (Fig. 8e) and NRLG2S (Fig. 9e) at geographical coordinates 20.85°S, 168.14°E. The background infrasound network used for synthetic data computation in different atmospheric configurations is composed of 360 arrays ranging from 180 to 600 km from the source at every 10° in azimuth.

For each atmospheric profile, we perform three inversions. The first inversion (hereafter abbreviated I-1) uses all synthetic detections. The second and third inversions (abbreviated I-2 and I-3) are performed using an arbitrary selection of 25 and 10 arrays among the arrays detecting the event. Figs. 6 and 7 show the infrasound arrays detecting the events for each inversion I-1, I-2 and I-3 and each atmospheric profile used for synthetic data generation. A map of ray endpoints colour coded according to the turning point altitude are also shown in each case. In addition, detected rays with turning point altitudes above ∼140 km are removed from the inversion procedure. Tables 1 and 2 synthesize the arrays and the corresponding detected phases for each inversion.

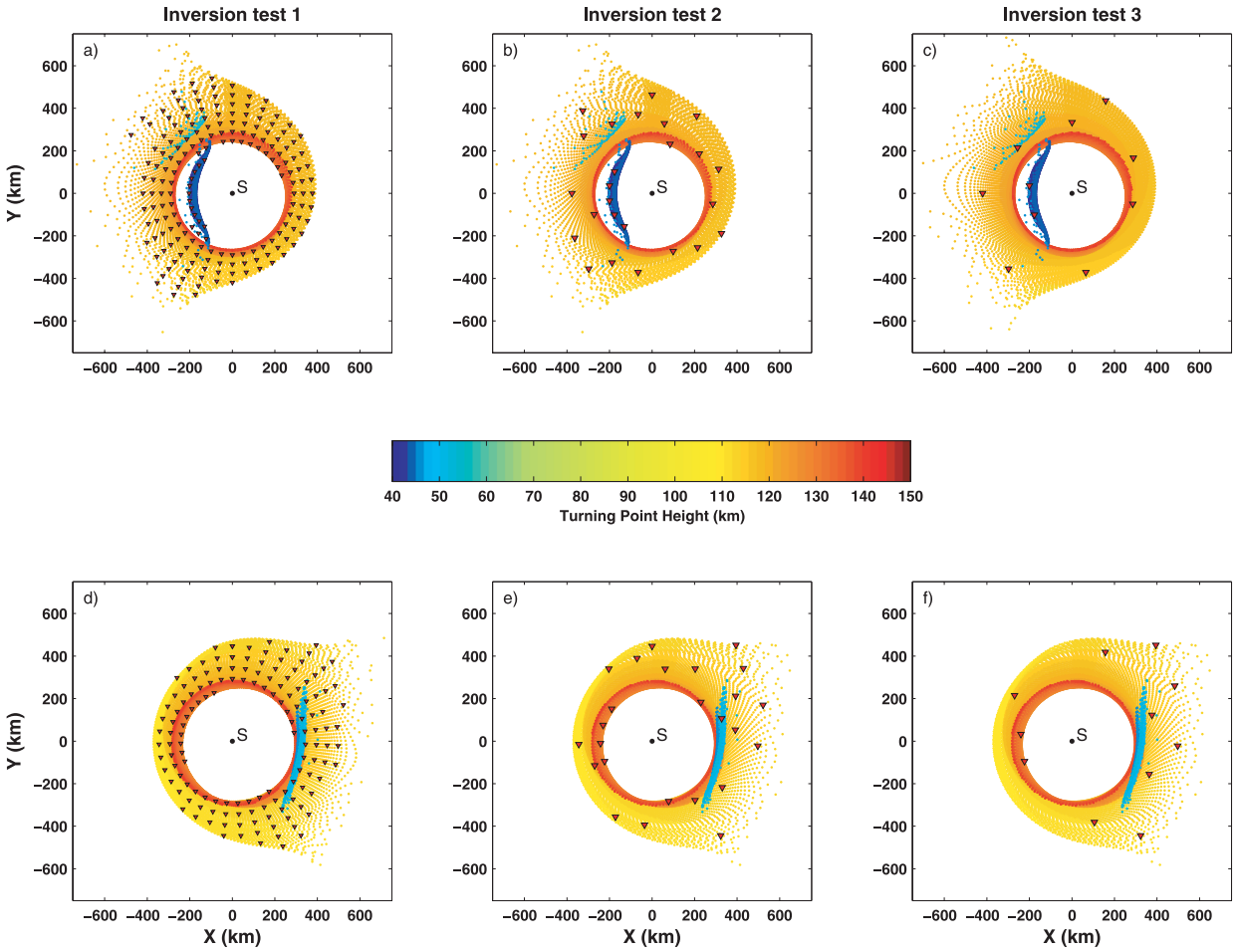

Figure 6. Synthetic array locations (triangles) used for each inversion of the HWM07 synthetic data set superimposed on the map of ray endpoints colour coded according to the turning point altitude. Maps of ray endpoints for the austral summer condition and location of 164 arrays (a), 25 arrays (b) and 10 arrays (c). Maps of ray endpoints for the equinox condition and location of 145 arrays (d), 25 arrays (e) and 10 arrays (f). The source (black dot) is located at $(x, y, z) = (0, 0, 0)$.

4.2 Details on the inverse procedure

4.2.1 The concept of a kinematically compatible model

The choice of a starting model is a critical step since it should be located in the vicinity of the global minimum. The starting model is generally chosen as the mean prior information on the atmospheric state which has to be set objectively. We introduce the concept of a kinematically compatible model as an atmospheric model that correctly predicts the observed infrasound phases (i.e. stratospheric and/or thermospheric phases). The iterative inverse algorithm converges towards a local minimum when mismodelled phases are present. Indeed, mismodelled phases behave as outliers in the data set for which least-squares methods are known to be non-robust. Meanwhile, a starting model that correctly predicts observed phases does not guarantee a convergence towards the global minimum.

4.2.2 Inversion initialization

For each inversion case, the starting models are the time-averaged mean of the corresponding season (Figs 8a & e and 9a & e). These models are likely kinematically incompatible with observations. To overcome these kinematic incompatibilities, the inversion is run with well-modelled phases for the first iterations until a correct prediction of all phases is obtained. Moreover, to stabilize the inversion procedure, the lowermost kilometres of the atmosphere (typically up to ∼15–20 km) are assumed to be known and remain unperturbed during the inversion procedure. This assumption is not excessively restrictive as atmospheric specifications are generally well resolved at these altitudes. In addition, Table 3 resumes the number of OBFs used to reconstruct zonal and meridional winds in each inversion case.

4.2.3 An heuristic method to improve the convergence

For each inversion, the weighting factor α of eq. (6) is logarithmically relaxed during the inversion procedure leading to an increasing weight of the data misfit term (6) with iteration. This is an heuristic method in contradiction with the probabilistic assumption behind the objective function (4) because it changes the covariance matrix $\mathbf{C}_m$ during the iterative procedure and is equivalent to changing the prior information at each iteration. However, such an heuristic method is justified because, in the case of synthetic data inversion, the model $\mathbf{m}_p$ does not represent a prior information on the atmospheric state in the sense of the probabilistic formulation. It is actually related to a critical starting model, from which we expect to

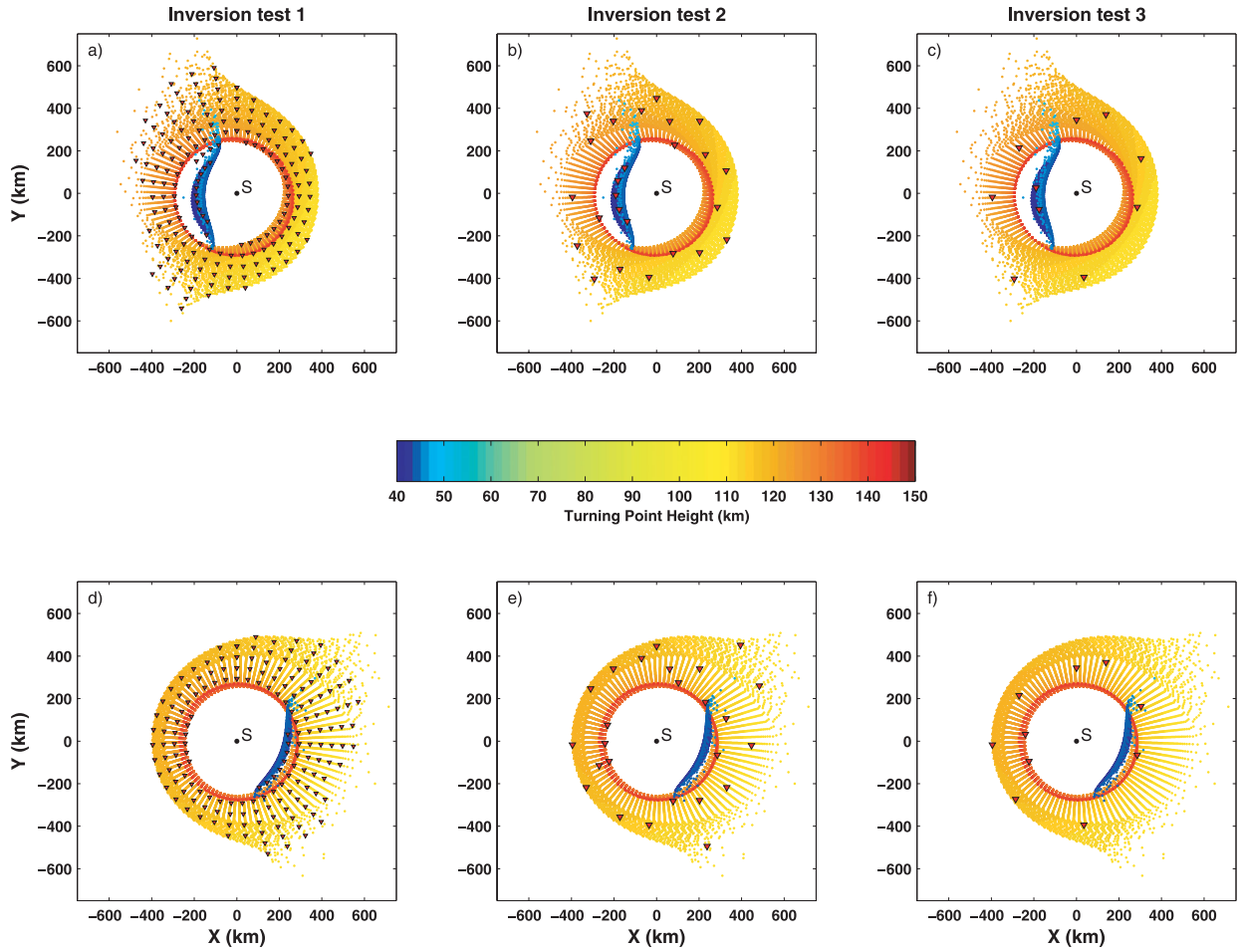

Figure 7. Synthetic array locations (triangles) used for each inversion of the NRLG2S synthetic data set superimposed on the map of ray endpoints colour coded according to the turning point altitude. Map of ray endpoints for the austral summer condition and location of 180 arrays (a), 25 arrays (b) and 10 arrays (c). Map of ray endpoints for the equinox condition and location of 173 arrays (d), 25 arrays (e) and 10 arrays (f). The source (black dot) is located at $(x, y, z) = (0, 0, 0)$.

Table 1. HWM07 synthetic data set used for validation of inverse algorithm. I-1 corresponds to inversion with the highest number of arrays, I-2 to 25 arrays and I-3 to 10 arrays.

	Summer			Equinox		
	I-1	I-2	I-3	I-1	I-2	I-3
Number of arrays	164	25	10	145	25	10
Is	28	6	3	7	1	1
It	169	20	8	145	25	11

Table 2. NRLG2S synthetic data set used for validation of inverse algorithm. I-1 corresponds to inversion with the highest number of arrays, I-2 to 25 arrays and I-3 to 10 arrays.

	Summer			Equinox		
	I-1	I-2	I-3	I-1	I-2	I-3
Number of arrays	180	25	10	173	25	10
Is	19	5	5	12	0	0
It	165	20	5	165	25	10

converge towards the true state. This is emphasized because starting models used in this study result in very large misfit values that may not be observed with real data sets (Antier *et al.* 2007; Ceranna *et al.* 2009; Hedlin *et al.* 2010), except in the presence of outliers in the data sets.

4.3 Inversion results with HWM07 specification

Synthetic data from summer conditions (Fig. 8a) result in 169 thermospheric and 28 stratospheric arrivals (Table 1). This atmospheric state typically corresponds to conditions where the starting model is likely kinematically incompatible with observations because of a strong sensitivity of thermospheric and stratospheric paths to the transition point. For instances, stratospheric arrivals can be modelled as thermospheric paths when the stratospheric wind jet is underestimated, while thermospheric paths are likely modelled as stratospheric paths when stratospheric wind jet is overestimated. In these cases, inversion starts with the compatible phases for the first iterations. The atmospheric profiles are successfully retrieved (Fig. 8b) in the case of the dense network of stations for both zonal and meridional fields. When decreasing the number of stations, the quality of the retrieval is affected but remain satisfying as mean error does not exceed $\sim$3.5 m s^{-1} (Table 4) for both zonal and meridional winds in the least favourable case (i.e. with 10 infrasound arrays).

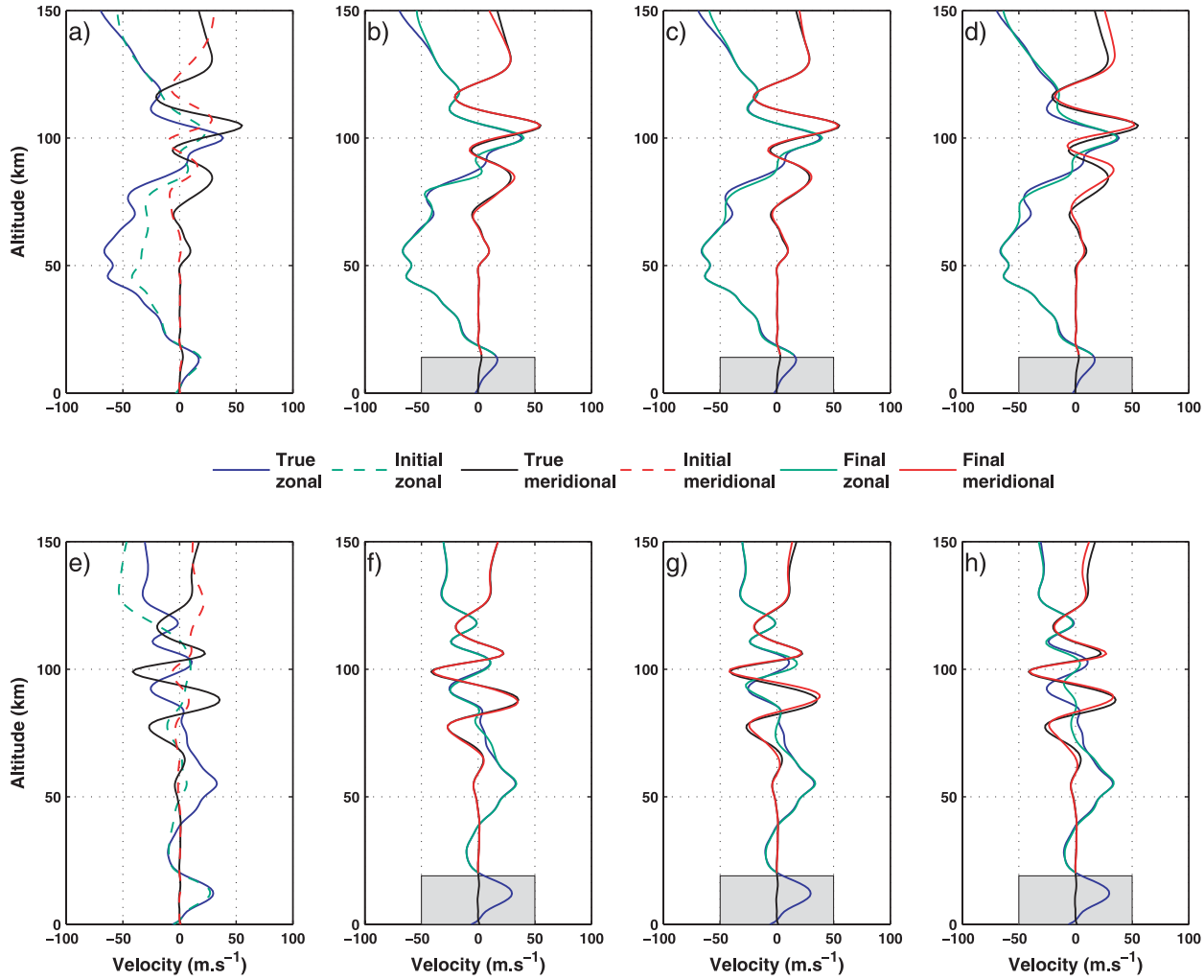

Figure 8. Inversion results from HWM07 synthetic data. (a) True summer wind profiles (solid lines) versus initial wind profiles (dashed lines). Retrieved profiles after inversion with 164 arrays (b), 25 arrays (c) and 10 arrays (d) versus true wind state. (e) True equinox wind profiles (solid lines) versus initial wind profiles (dashed lines). Retrieved profiles after inversion with 145 arrays (f), 25 arrays (g) and 10 arrays (h) versus true wind state. Grey rectangles correspond to the section of wind profiles not inverted.

In addition, the overall wind field structure is always successfully recovered.

Equinox atmospheric profiles (Fig. 8e) are characterized by wind amplitudes significantly lower than summer conditions (Fig. 8a), especially at stratospheric altitudes. This results in wind profiles where weak amplitude variabilities have a great importance in the overall wind structures. We observed that more OBFs and latent variables are needed to reconstruct the atmospheric profiles (Table 3). The inversion can therefore become unstable as higher order basis functions correspond to more oscillating eigenvectors of the covariance matrix (27). In this case, convergence is ensured by adequately setting the weighting parameter α. The retrieved profiles are satisfactory despite the increased number of unknown parameters. As expected, the decreasing number of infrasound arrays affects the inversion retrieval by increasing the mean error in the retrieved atmospheric profiles (Table 4).

Finally, we note that mean error in retrieved summer meridional profile decreases between the first and second inversion from 0.68 to 0.57 m s^{-1}. This may seem surprising as the number of infrasound arrays decreases from 164 to 25 between the first and second inversion. This is due to a better meridional retrieval above 120 km, that is, altitudes not reached by ray paths.

4.4 Inversion results with NRLG2S specification

The inversions of synthetic data computed with NRLG2S specifications lead to the same conclusions as those derived from the HWM07 related data set. NRLG2S atmospheric specifications which use NWP model up to ∼50 km, contain more detail compared with HWM07. These fine-scale vertical structures require an increasing number of OBFs (see Table 3) to describe the NRLG2S profiles with an accuracy equivalent to that of HWM07. In addition, we also note that equinox conditions require more OBFs than profiles from austral summer conditions (Table 3). Fig. 9 summarizes the results of the six inversions made for summer and equinox conditions. As for HWM07, the general structure of atmospheric profiles are well retrieved for both zonal and meridional winds. The mean error of the retrieved profiles (Table 4) increases with a decreasing number of infrasound arrays with an exception for zonal wind retrieval

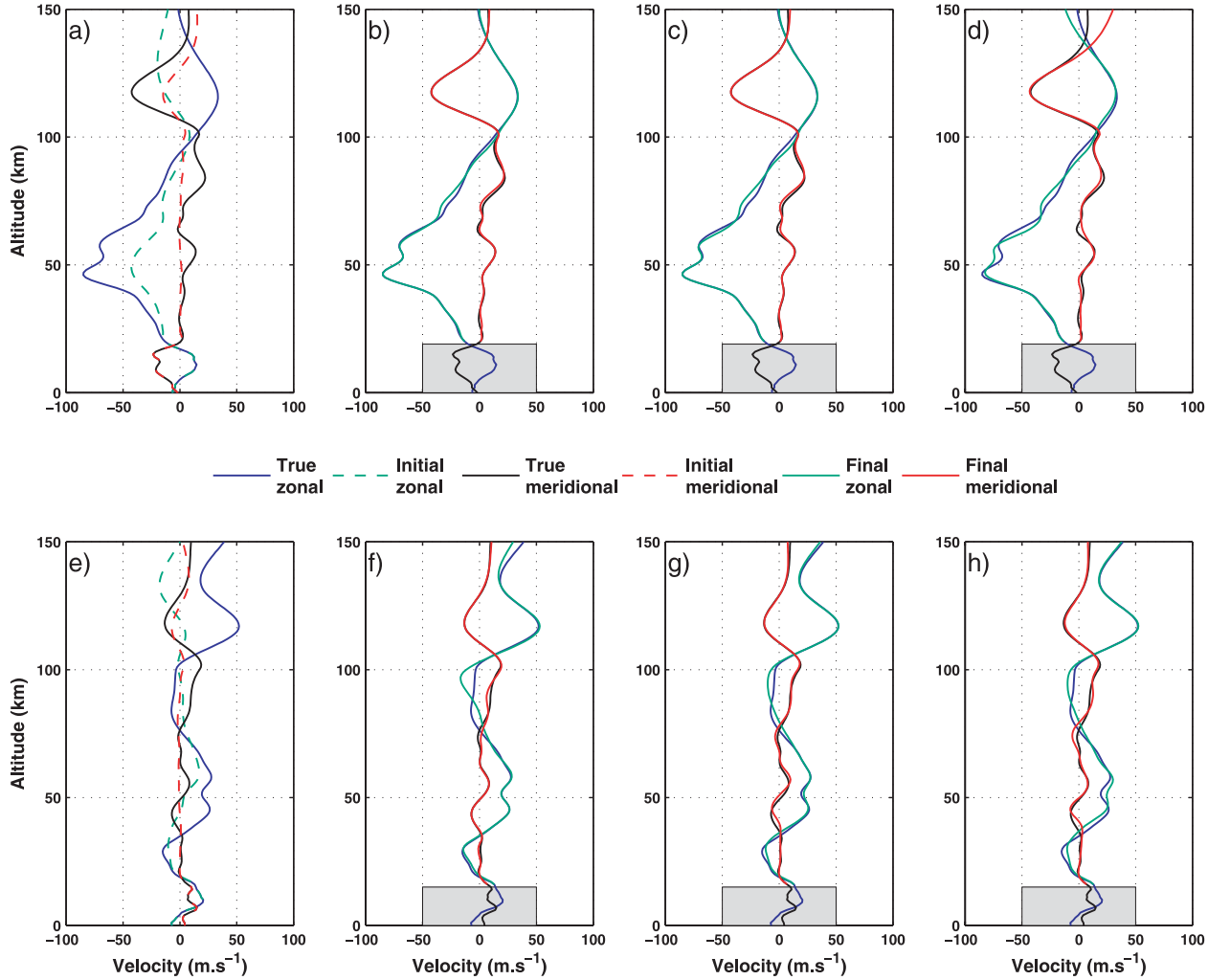

Figure 9. Inversion results from NRLG2S synthetic data. (a) True summer wind profiles (solid lines) versus initial wind profiles (dashed lines). Retrieved profiles after inversion with 180 arrays (b), 25 arrays (c) and 10 arrays (d) versus true wind state. (e) True equinox wind profiles (solid lines) versus initial wind profiles (dashed lines). Retrieved profiles after inversion with 173 arrays (f), 25 arrays (g) and 10 arrays (h) versus true wind state. Grey rectangles correspond to the section of wind profiles not inverted.

Table 3. Number of OBF used to reconstruct zonal and meridional wind profiles for each inversion. I-1 corresponds to inversion with the highest number of arrays, I-2 to 25 arrays and I-3 to 10 arrays.

	Summer			Equinox		
	I-1	I-2	I-3	I-1	I-2	I-3
HWM07	17	17	17	20	20	20
NRLG2S	19	19	19	21	21	21

Table 4. Mean error (in m s^{-1}) of the retrieved wind profiles for the 12 synthetic inversions. I-1 corresponds to inversion with the highest number of arrays, I-2 to 25 arrays and I-3 to 10 arrays.

		Summer			Equinox		
		I-1	I-2	I-3	I-1	I-2	I-3
HWM07	Zonal	1.32	1.51	3.00	1.00	1.47	2.97
	meridional	0.68	0.57	3.28	0.62	1.86	2.01
NRLG2S	Zonal	1.08	1.45	2.63	2.29	1.78	2.52
	meridional	0.73	0.76	1.88	0.75	1.07	1.40

during the equinox which has an abnormally high mean error of 2.29 m s^{-1} after inversion I-1 (composed of 173 arrays). This is mainly explained by the poor retrieval of zonal wind between 75 and 100 km which can be due to the presence of local minima. The use of Monte Carlo sampling of the parameter space may help to understand this feature. The corresponding retrievals for inversion I-2 and I-3 are significantly better at these altitudes.

The mean error of retrieved profiles from NRLG2S and HWM07 specifications are not comparable as we do not use the same infrasound network for each inversion experiments and the weighting parameter α controlling the relative weight between data fit and prior model fit is specific to each inversion.

5 DISCUSSION

In this section some features of infrasound atmospheric sounding arising from the synthetic inversion experiments are discussed. We discuss some aspects of the convergence, as well as implications of the simplifications and assumptions made.

We introduce the weighting parameter α in eq. (6), which controls the trade-off between data fit and prior model fit. Increasing this coefficient gives more weight to the prior model and slows down the convergence rate. Consequently, more iterations are needed to obtain a satisfying data fit. Most of the instabilities encountered in the inversion can be avoided by properly setting this parameter. In the probabilistic formulation of the objective function, this weighting factor should actually be incorporated inside the covariance matrix $\mathbf{C}_m$. However, this formulation makes it easier to change the trade-off between data and model misfit and helps to stabilize the inversion.

Ray tracing methods are strongly sensitive to the transition point between stratospheric and thermospheric paths (Drob *et al.* 2010). At this transition point, ray tracing methods are discontinuous and both stratospheric and thermospheric branches diverge asymptotically towards infinity. The related infrasound phases are subject to strong geometrical spreading. In this domain, the stratospheric phases correspond physically to the fast stratospheric arrivals (Evers & Haak 2007) while thermospheric phases cannot be observed due to the strong attenuation by geometrical expansion. In the vicinity of this transition point, both forward and inverse problems are non-linear, and this is the point where linear inversion methods breakdown. Mathematically, it is due to the non-differentiability of the forward problem. To avoid instability of the inversion caused by this non-linearity, we attempt to prevent phase conversions during the inverse procedure. This is done by a proper choice of prior model weight and introducing regularization terms to avoid strong perturbation of the wind model. The main limit of our algorithm in this regard is the same as every linear inversion algorithm and depends on the choice of starting model. In Section 4.2 we introduced the concept of a kinematically compatible model, which is characterized by predicted infrasound phases compatible with observations. Incompatible starting models result in a convergence towards a local minimum. This can be avoided by running the inversion using only well-modelled phases for the first iterations provided that infrasound phases can be identified without confusion.

Atmospheric profiles from NRLG2S specifications are not retrieved as easily as profiles from the HWM07 model. The inversion of NRLG2S synthetic data requires generally more iterations than inversion from HWM07 synthetic data. This result was expected since NRLG2S contains vertical fine-scale structures that are not present in the HWM07 wind model. The vertical complexity is better retrieved by increasing the number of orthogonal functions and latent variables. However, empirical orthogonal functions of higher order contain higher frequency oscillations, resulting in a possibly unstable inversion procedure. These instabilities can be easily handled by adjusting the weighting parameter α.

The number of stations and their positions strongly affects the inversion results. To illustrate these features, we have shown the impact of a reduced number of infrasound arrays on the inversion. Ideally, the array network should cover different range and azimuths. A poor coverage in azimuth and propagation range will, as expected, result in poor retrieval of wind parameters. Azimuthal coverage is important, as it allows handling the anisotropic nature of infrasound atmospheric sounding due to wind directivity. Range coverage is important for distributing sensitivity to the wind model at different altitudes.

In this study, we have considered the ideal case of noise-free data to highlight main issues of the infrasound inversion algorithm. The present algorithm is based on the assumption of Gaussian uncertainties over the data space. Departure from this assumption may occur with real data and could lead to a convergence towards a local minimum. Different statistical laws or error norm should be investigated in the presence of noisy data to find the formulation appropriate to infrasound observations.

The spatiotemporal variability of the atmosphere is a key feature in the understanding of infrasound propagation. Ray tracing is adapted to model large-scale atmospheric effects on infrasound propagation; this includes the day-to-day variability due to planetary waves and ray path changes due to migrating solar tides. Indeed, the infrasound wavefield is strongly influenced by various scales of variability of the atmospheric system, including the general circulation, seasonal changes, diurnal fluctuation due to planetary waves, migrating and non-migrating solar tides and gravity waves. Atmospheric effects such as gravity waves and turbulence in the boundary layer are known to produce scattering of the acoustic energy that are not modelled in the high-frequency approximation of the wave equation. Specific methods based on full-waveform modelling are required to reproduce these scattering effects (Millet *et al.* 2007).

In addition, we assume a range-independent atmosphere and Cartesian geometry for numerical simplification. Considering this, we state that this inversion algorithm is well suited to regional application, that is, propagation range up to 700 km. Application to long-range propagation would require the forward problem to be converted into spherical coordinate. Though there is no mathematical difficulty in using spherical coordinates, this algorithm is developed in a Cartesian frame for simplification and because it is inconceivable, with the current infrasound network, to perform inversion on long-range propagation. Indeed, long-range propagation is subject to 3-D/4-D propagation effects and requires the use of 3-D/4-D atmospheric models, increasing drastically the amount of unknown parameters. This increase in unknown model parameters has to be counter-balanced by an increase in infrasound observations to track the 3-D/4-D propagation effects.

Several ground truth event studies with high spatial coverage of infrasound receivers have been conducted to characterize infrasound propagation. The 1987 Misty picture experiment (New Mexico, USA) for which 23 sensors were deployed up to a range of 1200 km (Reed *et al.* 1987; Blanc 1988), is a unique data set in terms of station coverage. However, wave front parameters such as trace velocity and azimuth, which are explicitly used in our inversion, are not available because infrasound receivers consisted of single sensor. Thus, the proposed algorithm is not adapted to invert this data set which requires the computation of eigenrays. Since this first experiment, infrasound calibration explosions have been conducted at the Sayarim Military Range, Israel, in 2009 August and 2011 January and instrumented by infrasound receivers in array configurations (Gitterman *et al.* 2011). In addition, similar experiments have been conducted at the Utah Test and Training Range (UTTR), United States, with a high spatial resolution of infrasound arrays (Talmadge *et al.* 2010). Due to the amount of infrasound arrays located at regional-scale distances, these data sets constitute an ideal starting point to perform infrasound atmospheric sounding.

We note that the quality of inverted atmospheric profiles greatly depends on the accuracy of the forward model in describing propagation physics. In this study, assumptions and simplifications were made to understand the behaviour of the different physical parameters in an inversion procedure. The consideration of more detailed physics in the infrasound propagation modelling, including amplitude evolution, non-linearity and frequency dependence, will increase the non-linearity of the inverse problem and, consequently, will have to be introduced progressively.

6 CONCLUSION

This study describes a new algorithm for infrasound atmospheric sounding. Our approach was motivated by recent infrasound studies, which have highlighted the potential of infrasound signal for global atmospheric studies, especially for improving the understanding of the mesosphere and lower thermosphere. However, rigorous development of inverse theory in the context of infrasound studies has not been extensively covered in the literature; Drob *et al.* (2010) have studied this problem in a context similar to this study.

The good agreement between inverted profiles and true profiles shows that our approach is appropriate for infrasonic atmospheric sounding. A specific parametrization of the unknown model parameters based on PCA is adopted, which naturally introduces some regularization of the inverse problem. Atmospheric sounding with infrasound data should be restricted to a regional scale, that is, propagation ranges less than 700 km from the source, which correspond to distances where atmospheric 3-D effects on the propagation are not too important, and where ray tracing can be used in Cartesian coordinates neglecting the Earth's sphericity. Furthermore, currently available infrasound network configurations do not allow infrasound tomography at a global scale.

We propose to use this algorithm to assess the performance of existing regional monitoring network as well as in the designing of regional infrasound observing system. Application to real data cases is possible, but may require additional work on robustness to noise level and uncertainty analysis (including correlation of uncertainties in the data covariance matrix $\mathbf{C}_D$), the error norm used in the misfit function (here an L_2-norm) and uncertainty distributions.

ACKNOWLEDGMENTS

The authors acknowledge Douglas P. Drob for providing the NRLG2S-HWM93 atmospheric specifications. Careful reviews from Olaf Gainville and two anonymous reviewers helped to improve the original manuscript. The authors are thankful to Jean Virieux for preliminary discussions about this work.

REFERENCES

Aki, K. & Richards, P., 1980. *Quantitative Seismology,* 2nd edn, Freeman, San Francisco, CA.

Antier, K., Le Pichon, A., Vergniolle, S., Zielinski, C. & Lardy, M., 2007. Multiyear validation of the NRL-G2S wind fields using infrasound from Yasur, *J. geophys. Res.,* **112,** D23110.

Balachandran, N.K., Donn, W.L. & Rind, D.H., 1977. Concorde sonic booms as an atmospheric probe, *Science,* **197,** 47–49.

Bass, H.E., Sutherland, L.C., Zuckerwar, A.J., Blackstock, D.T. & Hester, D.M., 1995. Atomospheric absorption of sound: further developments, *J. acoust. Soc. Am.,* **97,** 680–683, doi:10.1121/1.412989.

Blanc, E., 1988. Mesures ionosphériques et microbarographiques-expérience misty picture. Technical Report 370/88, CEA.

Bordoni, S. & Stevens, B., 2006. Principal component analysis of the Summertime Winds over the Gulf of California: a Gulf Surge Index, *Mon. Weather Rev.,* **134,** 3395–3414.

Campus, P. & Christie, D.R., 2010. Worldwide observations of Infrasonic Waves, in *Infrasound Monitoring for Atmospheric Studies,* ch. 6, Springer, Dordrecht.

Candel, S., 1977. Numerical solution of conservation equations arising in linear wave theory: application to aeroacoustics, *J. Fluid Mech.,* **83,** 465–493.

Cansi, Y., 1995. An automatic seismic event processing for detection and location: the PMCC method, *Geophys. Res. Lett.,* **22,** 1081–1125.

Ceranna, L., Le Pichon, A., Green, D.N. & Mialle, P., 2009. The Buncefield explosion: a benchmark for infrasound analysis across Central Europe, *Geophys. J. Int.,* **177,** 491–508.

Courant, R. & Hilbert, D., 1989. *Methods of Mathematical Physics,* Volume II, Wiley Interscience, New York, NY.

Courtier, P. *et al.*, 1998. The ECMWF implementation of three-dimensional variational assimilation (3D-Var) I: formulation, *Q. J. R. Meteorol. Soc.,* **124,** 1783–1807.

De Boor, C., 1978. *A Practical Guide to Splines,* Springer-Verlag, New York, NY.

Delclos, C., Blanc, E., Broche, P., Glangeaud, F. & Lacoume, J.L., 1990. Processing and interpretation of microbarograph signals generated by the explosion of Mount St. Helens, *J. geophys. Res.,* **95,** 5485–5494.

Delprat-Jannaud, F. & Lailly, P., 1995. Reflection tomography: how to handle multiple arrivals? *J. geophys. Res.,* **100,** 703–715.

Dessa, J.-X., Virieux, J. & Lambotte, S., 2005. Infrasound modeling in a spherical heterogeneous atmosphere, *Geophys. Res. Lett.,* **32,** L12808, doi:10.1029/2005GL022867.

Donn, W. & Rind, D., 1971. Natural infrasound as an atmospheric probe, *Geophys. J. R. astr. Soc.,* **26,** 111–133.

Drob, D.P., Picone, J.M. & Garcès, M., 2003. Global morphology of infrasound propagation, *J. geophys. Res.,* **108,** 4680, doi:10.1029/2002JD003307.

Drob, P.D. *et al.*, 2008. An empirical model of the earth's horizontal wind fields: HWM07, *J. geophys. Res.,* **113,** A12304, doi:10.1029/2008JA013668.

Drob, P.D., Meier, R.R., Picone, J.M. & Garcès, M.M., 2010. Inversion of infrasound signals for passive atmospheric remote sensing, in *Infrasound Monitoring for Atmospheric Studies,* ch. 24, Springer, Dordrecht.

Evers, L.G. & Haak, H.W., 2005. The detectability of infrasound in the Netherlands from the Italian volcano Mt. Etna, *J. Atmos. Sol.-Terr. Phys.,* **67,** 259–268.

Evers, L.G. & Haak, H.W., 2007. Infrasonic forerunners: exceptionally fast acoustic phases, *Geophys. Res. Lett.,* **34,** L10806, doi:10.1029/2007GL029353.

Farra, V., Virieux, J. & Madariaga, R., 1989. Ray perturbation theory for interfaces, *Geophys. J. Int.,* **99,** 377–390.

Fee, D., Garces, M. & Steffke, A., 2010. Infrasound from Tungurahua Volcano 2006-2008: Strombolian to Plinian eruptive activity, *J. Volc. Geotherm. Res.,* **193,** 67–81.

Gainville, O., Piserchia, P.-F., Blanc-Benon, P. & Scott, J., 2006. Ray tracing for long range atmospheric propagation of infrasound, in *Proceedings of 12th AIAA/CEAS Aeroacoustics Conference,* Cambridge, MA AIAA Paper No. 2006–2451.

Garcés, M., Hansen, R.A. & Lindquist, K.G., 1998. Traveltimes for infrasonic waves propagating in a stratified atmosphere, *Geophys. J. Int.,* **135,** 255–263.

Garcés, M., Iguchi, M., Ishihara, K., Morissey, M., Sudo, Y. & Tsutsui, T., 1999. Infrasonic precursors to a vulcanian eruption at Sakurajima Volcano, Japan, *Geophys. Res. Lett.,* **26,** 2537–2540.

Garcés, M., Aucan, J., Fee, D., Caron, P., Merrifield, M., Gibson, R., Bhattacharyya, J. & Shah, S., 2006. Infrasound from large surf, *Geophys. Res. Lett.,* **33,** L05611, doi:10.1029/2005GL025085.

Gitterman, Y., Given, J., Coyne, J., Zerbo, L. & Hofstetter, R., 2011. Large-scale explosion sources at Sayarim, Israel, for infrasound calibration of the International Monitoring System, *in Conference on Comprehensive Nuclear-Test-Ban Treaty: Science and Technology,* Vienna, Austria, 2011 June 8–10.

de Groot-Hedlin, C.D., 2008. Finite-difference time-domain synthesis of infrasound propagation through an absorbing atmosphere, *J. acoust. Soc. Am.,* **124,** 1430–1441.

Hagerty, M.T., Kim, W.-Y. & Martysevich, P., 2002. Infrasound detection of large mining blasts in Kazakstan, *Pure appl. Geophys.,* **159,** 1063–1079.

Hansen, C., 1992. Analysis of discrete ill-posed problems by means of the L-curve, *SIAM Rev.,* **34,** 561–580.

Hauchecorne, A., Keckhut, P. & Chanin, M.-L., 2010. Dynamics and transport in the middle atmosphere using remote sensing techniques from ground and space, in *Infrasound Monitoring for Atmospheric Studies,* ch. 22, Springer, Dordrecht.

Hedin, A.E., 1991. Extension of the MSIS thermosphere model into the middle and lower atmosphere, *J. geophys. Res.,* **96,** 1159–1172.
Hedin, A.E. *et al*., 1996. Empirical wind model for the upper, middle and lower atmosphere, *J. Atmos. Terr. Phys.,* **58,** 1421–1447.
Hedlin, M.A.H., Drob, D., Walker, K.T. & C. de Groot-Hedlin, C., 2010. A study of acoustic propagation from a large bolide in the atmosphere with a dense seismic network, *J. geophys. Res.,* **115,** B11312, doi:10.1029/2010JB007669.
Hogan, T.F. & Rosmond, T.E., 1991. The description of the navy operational global atmospheric prediction systems spectral forecast model, *Mon. Weather Rev.,* **119,** 1786–1815.
Julian, B.R. & Gubbins, D., 1977. Three dimensional seismic ray tracing, *J. Geophys.,* **43,** 95–114.
Kalnay, E., Kanamitsu, M. & Baker, W.E., 1990. Global numerical weather prediction at the National-Meteorological-Center, *Bull. Am. Meteorol. Soc.,* **71,** 1410–1428.
Le Pichon, A., Garcés, M., Blanc, E. & Barthélémy, M., 2002. Acoustic propagation and atmosphere characteristics derived from infrasonic waves generated by the Concorde, *J. acoust. Soc. Am.,* **111,** 629–641.
Le Pichon, A., Maurer, V., Raymond, D. & Hyvernaud, O., 2004. Infrasound from ocean waves observed in Tahiti, *Geophys. Res. Lett.,* **31,** L19103, doi:10.1029/2004GL020676.
Le Pichon, A., Blanc, E. & Drob, D.P., 2005a. Probing high-altitude winds using infrasound. *J. geophys. Res.,* **110,** D20104, doi:10.1029/2005JD006020.
Le Pichon, A., Blanc, E., Drob, D.P., Lambotte, S., Dessa, J.-X., Lardy, M., Bani, P. & Vergniolle, S., 2005b. Infrasound monitoring of volcanoes to probe high-altitude winds, *J. geophys. Res.,* **110,** D13106, doi:10.1029/2004JD005587.
Le Pichon, A., Blanc, E. & Hauchecorne, A., 2010. *Infrasound Monitoring for Atmospheric Studies,* 1st edn, Springer, Dordrecht.
Lingevitch, J.F., Collins, M.D., Mills, M.J. & Evans, R.B. & Siegmann, W.L., 2002. A wide angle and high Mach number parabolic equation, *J. acoust. Soc. Am.,* **111,** 729–734.
Levenberg, K., 1944. A method for the solution of certain problems in least squares, *Quart. appl. Math.,* **2,** 164–168.
Marquardt, D., 1963. An algorithm for least-squares estimation of nonlinear parameters, *SIAM, J. appl. Math.,* **11,** 431–441.
Marty, J., Ponceau, D. & Dalaudier, F., 2010. Using the International Monitoring System infrasound network to study gravity waves, *Geophys. Res. Lett.,* **37,** L19802, doi:10.1029/2010GL044181.
Matoza, R.S., 2009. Seismic and infrasonic source processes in volcanic fluid systems, *PhD thesis*, University of California, San Diego.
Matoza, R.S., Fee, D., Garces, M., Seiner, J.M., Ramon, P.A. & Hedlin, M.A.H., 2009. Infrasonic jet noise from volcanic eruptions, *Geophys. Res. Lett.,* **36,** L08303, doi:10.1029/2008GL036486.
Matoza, R.S., Le Pichon, A., Vergoz, J., Herry, P., Lalande, J.-M., Lee, H. I., Che, I.-Y. & Rybin, A., 2011. Infrasonic observations of the June 2009 Sarychev Peak eruption, Kuril Islands: implications for infrasonic monitoring of explosive volcanism, *J. Volc. Geotherm. Res.,* **200,** 35–48.
Millet, C., Robinet, J.-C. & Roblin, C., 2007. On using computational aeroacoustics for long-range propagation of infrasounds in realistic atmospheres, *Geophys. Res. Lett.,* **34,** L14814, doi:10.1029/2007GL029449.
Monteiller, V., Got, J.-L., Virieux, J. & Okubo, P., 2005. An efficient algorithm for double-difference tomography and location in heterogeneous media, with an application to the Kilauea volcano, *J. geophys. Res.,* **110,** B12306, doi:10.1029/2004JB003466.
Munk, W., Worcester, P. & Wunsch, C., 1995. *Ocean Acoustic Tomography,* Cambridge University Press, Cambridge.
Mutschlecner, J. P. & Whitaker, R. W., 2005. Infrasound from earthquakes, *J. geophys. Res.,* **110,** D01108, doi:10.1029/2004JD005067.
Nolet, G., 1987. *Seismic Tomography,* Reidel, Dordrecht, The Netherlands.
Ostashev, V.E., Juvé, D. & Blanc-Benon Ph., 1997. Derivation of a wide angle parabolic equation for sound waves in inhomogeneous moving media, *Acta acuost. United with Acustica,* **83,** 455–460.
Paige, C.C. & Saunders, M.A., 1982. LSQR: sparse linear equations and least-squares problems, *ACM Trans. Math. Softw.,* **8,** 195–209.
Pierce, A.D., 1967. Guided Infrasonic Modes in a Temperature- and Wind-Stratified Atmosphere, *J. acoust. Soc. Am.,* **41,** 597–611.
Pierce, A.D., 1994. *Acoustics: An Introduction to its Physical Principles and Applications,* 3rd edn, Acoust. Soc. Am., New York, NY.
Reed, J.W., Church, H.W. & Huck, T.W., 1987. Misty picture weather-watch and microbarograph project: experiments 9412–14-18. Sand-201387-2978c, Sandia National Laboratories.
Shampine, L.F. & Gordon, M.K., 1975. *Computer Solution of Ordinary Differential Equations: The Initial Value Problem,* W. H. Freeman, San Francisco, CA.
Spiesberger, J.L. & Worcester, P.F., 1983. Perturbations in travel time and ray geometry due to mesoscale disturbances: a comparison of exact and approximate calculations, *J. acoust. Soc. Am.,* **74,** 219–225.
Sutherland, L.C. & Bass, H.E., 2004. Atmospheric absorption in the atmosphere up to 160 km, *J. acoust. Soc. Am.,* **115,** 1012–1032.
Talmadge, C.L., Waxler, R., Kleinert, D., Nava, S., Assink, J., Buchanan, H., Carpenter, B. & Heffington, J., 2010. A large scale infrasound array deployment in the American West, Am. geophys. Un., Fall Meeting, Poster S11A-1923.
Tarantola, A., 2005. *Inverse Problem Theory and Methods for Model Parameter Estimation,* SIAM, Philadelphia, PA.
Virieux, J. & Farra, V., 1991. Ray-tracing in 3-D complex isotropic media: an analysis of the problem, *Geophysics,* **56,** 2057–2069.
Virieux, J., Garnier, N., Blanc, E. & Dessa, J.-X., 2004. Paraxial ray tracing for atmospheric wave propagation, *Geophys. Res. Lett.,* **31,** L20106, doi:10.1029/2005GL020514.
Whitham, G.B., 1999. *Linear and Nonlinear Waves*. Wiley, New York, NY.
Williams, C.R., 1997. Principal component analysis of wind profiler observations, *J. Atmos. Ocean. Tech.,* **14,** 386–395.
Wilson, C.R., 1969. Auroral infrasonic waves, *J. geophys. Res.,* **74,** 1812–1836.
Wilson, C.R. & Nichparenko, S., 1967. Infrasonic waves and auroral activity, *Nature,* **214,** 1299–1302.

APPENDIX: PARTIAL DERIVATIVES OF THE HAMILTONIAN FUNCTION

Analytical expressions used for the ray tracing equations are

$$\frac{\partial \mathcal{H}}{\partial q_i} = -\frac{1}{2}\Omega \frac{\partial u^2}{\partial q_i} + u^2 \Omega p_l \frac{\partial v_l}{\partial q_i}, \tag{A1}$$

and

$$\frac{\partial \mathcal{H}}{\partial p_i} = p_i + u^2 \Omega v_i, \tag{A2}$$

where $\Omega = 1 - p_k v_k$. Second partial derivatives used in the paraxial system (14) and perturbed system are

$$\frac{\partial^2 \mathcal{H}}{\partial p_i \partial p_j} = \delta_{ij} - v_i v_j u^2, \tag{A3}$$

$$\frac{\partial^2 \mathcal{H}}{\partial p_i \partial q_j} = u^2 \Omega \frac{\partial v_i}{\partial q_j} + \Omega v_i \frac{\partial u^2}{\partial q_j} - u^2 v_i p_k \frac{\partial v_k}{\partial q_j} \tag{A4}$$

$$\frac{\partial^2 \mathcal{H}}{\partial q_i \partial q_j} = -\frac{1}{2}\Omega^2 \frac{\partial^2 u^2}{\partial q_i \partial q_j} + \Omega \frac{\partial u^2}{\partial q_i} p_l \frac{\partial v_l}{\partial q_i} - u^2 \times \left(p_l \frac{\partial v_l}{\partial q_j}\right)\left(p_l \frac{\partial v_l}{\partial q_i}\right) + u^2 \Omega p_l \frac{\partial^2 v_l}{\partial q_i \partial q_j}. \tag{A5}$$

The perturbation $\Delta\mathcal{H}$ of the Hamiltonian due to a unit perturbation of wind model, δv, is

$$\Delta\mathcal{H} = u^2 p_i \delta v_i (1 - p_i v_i). \tag{A6}$$

Partial derivatives of the perturbed Hamiltonian $\Delta\mathcal{H}$ are

$$\frac{\partial \Delta\mathcal{H}}{\partial p_i} = u^2(\delta v_i p_j \delta v_j - v_i p_j \delta v_j), \tag{A7}$$

and

$$\frac{\partial \Delta\mathcal{H}}{\partial q_i} = \frac{\partial u^2}{\partial q_i} p_j v_j p_k \delta v_k + u^2 \left(p_j v_j p_k \frac{\partial \delta v_k}{\partial q_i} - p_j \delta v_j p_k \frac{\partial v_k}{q_i} \right). \tag{A8}$$

In each case, the Einstein sommation convention is used.